

Quantum anomalous, quantum spin, and quantum valley Hall effects in pentalayer rhombohedral graphene

Koji Kudo,¹ Ryota Nakai,^{1,2} and Kentaro Nomura¹

¹*Department of Physics, Kyushu University, Fukuoka 819-0395, Japan*

²*RIKEN Center for Quantum Computing (RQC), Wako, Saitama, 351-0198, Japan*

Recent experiments in pentalayer rhombohedral graphene moiré superlattice have observed the quantum anomalous Hall effect at the moiré filling factor $\nu = 1$ and various fractions. These effects result from a flat Chern band induced by electron-electron interactions. In this Letter, we show that the many-body effects at $\nu = 2$ give rise to the quantum spin Hall and quantum valley Hall states, even without spin-orbit couplings or valley-dependent potentials, in addition to the quantum anomalous Hall state. These three topological states can be selectively induced by applying and tilting a magnetic field. Furthermore, we demonstrate that at $\nu = 3$ and 4, a combination of the Wigner-like crystal state and topological states can be the ground state. Consequently, the relation between states at the filling factor ν and its particle-hole counterpart $4 - \nu$ breaks down, which contrasts with the conventional quantum Hall effect in graphene.

Introduction. — The recent observation of the integer and fractional quantum anomalous Hall (QAH) effects in moiré materials [1–5] is a significant advancement in condensed matter physics. Moiré materials are a platform of strong interaction effects [6, 7], resulting in a variety of symmetry-broken phases such as superconductivity and Wigner crystals [8–12], as well as topological phases [13–18]. The QAH effect arises from the interplay of symmetry breaking and topology, where the Hall conductance is quantized even without external magnetic fields [19–22]. Among moiré materials, the integer and fractional QAH effects has been first observed in twisted bilayer MoTe₂ [1–4]. Recently, the QAH states in pentalayer rhombohedral graphene on hexagonal boron nitride (hBN) at the moiré filling factor $\nu = 1$ and some fractions have been reported [5]. Following up this breakthrough, intense theoretical effort has been made [23–45].

Chern bands in pentalayer rhombohedral graphene on hBN emerge from the interplay of three factors: layer stacking, moiré structure, and many-body interactions. In turn, the band touching at the charge-neutral point of multilayer rhombohedral graphene [46–56] becomes flatter ($\sim k^{N_L}$ with the wave number k) as the number of stacked layer N_L increases [57]. Moiré superlattice structure due to lattice mismatch between pentalayer graphene and hBN [58, 59] reduces the graphene’s Brillouin zone into the moiré one, making the band width smaller. Finally, the electron-electron interactions single out a Chern band from the rest of the moiré bands. Specifically, the Hartree-Fock (HF) analysis revealed the emergence of an isolated and nearly flat Chern band at $\nu = 1$ [31–34], which is absent without interaction. This mechanism is supposed to underlie the observed $\nu = 1$ and fractional QAH states [5, 31–33].

In general, quantum Hall physics [60–72] is based on *noninteracting* topological bands like the Landau level as a starting point, including integer and fractional Chern insulators [18, 73–77]. However, pentalayer rhombohedral graphene on hBN falls outside of this framework,

suggesting potentials for interaction-driven exotic phases beyond the conventional quantum Hall paradigm even at integer fillings. This motivates us to explore pentalayer rhombohedral graphene on hBN at integer fillings other than $\nu = 1$, which have not yet been reported in experiments under a sufficiently strong displacement field [5].

In this Letter, we show that pentalayer rhombohedral graphene at $\nu = 2$ can yield the quantum spin Hall (QSH) and quantum valley Hall (QVH) states, even without spin-orbit couplings or valley-dependent potentials, in addition to the QAH state. They emerge purely from many-body effects, as in the topological Mott insulator [78]. Our self-consistent HF calculation shows that the QAH, QSH, and QVH states at $\nu = 2$ are degenerate, while they are distinguishable by the magnitude of magnetization. This difference allows selective induction of one of the three states by applying and tilting magnetic fields, as shown in Fig. 1(a). The appearance of the three states can be understood from the analogy of $\nu = 1$: the emergent Chern band at $\nu = 1$ spontaneously selects the valley K, K' and spin \uparrow, \downarrow , where the Chern number is +1 (–1) for K (K') [31–34]. The ground state at $\nu = 2$ is composed of two Chern bands out of $(K\uparrow, K\downarrow, K'\uparrow, K'\downarrow)$ [see Fig. 1(b)]. Different combinations carry different topological numbers, leading to the QAH, QSH, and QVH states. All possible cases are summarized in Table I.

Remarkably, the empirical rule of forming the lowest energy state by occupying the Chern bands breaks down at $\nu = 3$ and 4. We find that at these fillings, a combination of the Wigner-like crystal (WLC) state and topological states can be the ground state. This happens because their spatial distributions of the charge density interlock with each other, that is, WLC’s localized density fits into low-density spots of topological states. Consequently, the ground states at $\nu = 3$ and 4 are not necessarily the particle-hole counterparts of $4 - \nu = 1$ and 0 within the Chern band subspace consisting of $(K\uparrow, K\downarrow, K'\uparrow, K'\downarrow)$. This property is a many-body effect as well, and contrasts

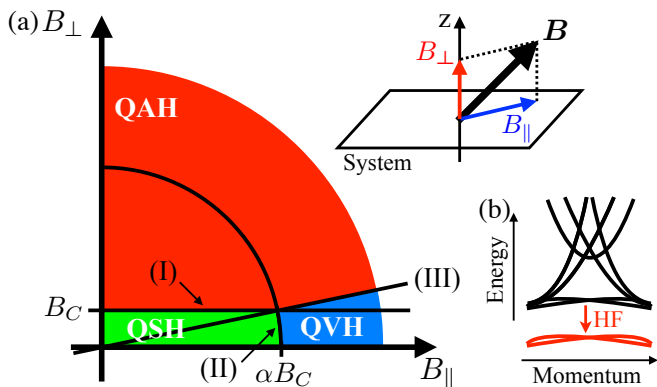


FIG. 1. (a) Lowest energy state as a function of in-plane and out-of-plane components (B_{\perp}, B_{\parallel}) of the magnetic field \mathbf{B} . Boundaries (I)-(III) are identified as follows: (I) QAH vs QSH: $B_{\perp} = B_C$. The critical magnetic field B_C is defined so that $B_C \times M_{\text{orb}}^z(\text{QAH})$, where M_{orb}^z is defined in Eq. (1), is equivalent to the magnetostatic energy of the QAH state. (II) QVH vs QSH: $|\mathbf{B}| = \alpha B_C$ with $\alpha = 4.9$ [see Eq. (2)]. (III) QVH vs QAH: $\alpha B_{\perp} = |\mathbf{B}|$. (b) Schematic of the band structure at $\nu = 2$. The HF interaction induces two isolated bands. As numerically demonstrated below, the selection of the valley and spin – specifically, any two from ($K\uparrow, K\downarrow, K'\uparrow, K'\downarrow$) – does not affect the total energy. All possible occupancies are summarized in Table I.

with the conventional quantum Hall effect in graphene.

Model — For numerical analysis, we use an effective continuum model [31, 33]. First we consider the tight-binding Hamiltonian of pentalayer rhombohedral graphene, including both intralayer and interlayer hoppings and the interlayer potential difference [See Sec. S1 in Supplementary Materials (SM) [79] for more details]. Employing a standard approach with a continuum limit, we obtain an effective Hamiltonian near the charge neutral point, $H_{R5G} = \sum_{\mathbf{k}} \mathbf{c}^{\dagger}(\mathbf{k}) h_{R5G}(\mathbf{k}) \mathbf{c}(\mathbf{k})$ for a given valley and spin, where $\mathbf{c}^{\dagger} = (c_{A_1}^{\dagger}, c_{B_1}^{\dagger}, c_{A_2}^{\dagger}, \dots, c_{B_5}^{\dagger})$ and $c_{X_l}^{\dagger}$ is a creation operator for the sublattice $X = A, B$ on the layer $l = 1, 2, \dots, 5$. Here, $h_{R5G}(\mathbf{k})$ is a 10-dimensional matrix. System parameters are set to match experimental conditions for the $\nu = 1$ QAH effect [5, 31, 33, 80].

Stacking graphene on hBN induces a moiré superlattice structure due to lattice mismatch. Here, we set the twist angle to 0.77° to align with the experiment in Ref. 5. Within the effective continuum model, the effect of hBN is represented by a local potential $v(\mathbf{r})$ within the bottom graphene subspace [58, 59] (see Sec. S2 in SM [79] for more details). Its second quantized form is $V_{\text{hBN}} = \sum_{\mathbf{k}} \sum_{m_1 m_2} \tilde{\mathbf{c}}^{\dagger}(\mathbf{k} + m_1 \mathbf{G}_1 + m_2 \mathbf{G}_2) v(m_1, m_2) \tilde{\mathbf{c}}(\mathbf{k})$, where $\tilde{\mathbf{c}}^{\dagger} = (c_{A_1}^{\dagger}, c_{B_1}^{\dagger})$, \mathbf{G}_1 and \mathbf{G}_2 the moiré reciprocal lattice vectors, and $v(m_1, m_2)$ is the Fourier coefficient of $v(\mathbf{r})$. In the numerical calculations, the summation $\sum_{\mathbf{k}} \sum_{m_1 m_2}$ is confined to the first and second moiré Brillouin zones.

Now we obtained an effective noninteracting Hamilto-

TABLE I. Possible occupancy of the four degrees of freedom at $\nu = 2$, yielding ${}_4C_2 = 6$ states. The charge Chern number C_c sums the band Chern numbers, while the spin (valley) Chern number C_s (C_v) calculates the difference regarding the spin (valley). [Here, the band Chern number for the valley K (K') is $+1$ (-1).] There are three types of states: quantum anomalous Hall (QAH), quantum spin Hall (QSH), and quantum valley Hall (QVH) states. The result for magnetization in Fig. 3 is also summarized. (o indicates finite magnetization.)

#	Occupancy				(C_c, C_s, C_v)	Type	Magnetization	
	$K\uparrow$	$K\downarrow$	$K'\uparrow$	$K'\downarrow$			Orbital	Spin
1	✓	✓	×	×	(2,0,2)	QAH	o	
2	×	×	✓	✓	(-2,0,2)			
3	✓	×	×	✓	(0,2,2)	QSH		
4	×	✓	✓	×	(0,-2,2)			
5	✓	×	✓	×	(0,0,2)	QVH		o
6	×	✓	×	✓	(0,0,2)			

nian as $H_{R5G} + V_{\text{hBN}}$. Then we add the HF interaction to incorporate many-body effects. The original interaction term is $H_{\text{int}} = (1/2S) \sum_{\mathbf{k}\mathbf{k}'\mathbf{q}} \sum_{ZZ'} V_C(\mathbf{q}) c_Z^{\dagger}(\mathbf{k} + \mathbf{q}) c_{Z'}^{\dagger}(\mathbf{k}' - \mathbf{q}) c_{Z'}(\mathbf{k}') c_Z(\mathbf{k})$, where S is the area of the system, and Z and Z' represent the spin, valley, sublattice, and layer indices. Here, we employ a dual gate-screened Coulomb interaction $V_C(\mathbf{q}) = e^2/(2\epsilon_0\epsilon_r q) \tanh(qd_s)$ for $\mathbf{q} \neq \mathbf{0}$ and $V_C(\mathbf{q} = \mathbf{0}) = 0$, with $d_s = 25\text{nm}$ as the gate distance and $\epsilon_r = 5$ as the dielectric constant [33]. See Sec. S3 in SM [79] for more details of the HF interaction. To reduce the computational cost, the following calculations are performed within the subspace of the first three noninteracting conduction bands for each valley and spin. We consider 24×24 moiré unit cells unless otherwise stated.

Band structure — Our self-consistent HF calculation assumes the spin and valley conservation. This assumption regarding spin is valid because of the SU(2) spin-rotational symmetry of the HF Hamiltonian. Similarly, the assumption regarding the valley is justified since superimposing K and K' gains additional energy [34].

Figures 2(a) and (b) show the HF band structures of the degenerate lowest energy solutions calculated by fixing the particle number with $\nu = 2$. In Fig. 2(a) [(b)], the occupied two lowest bands, distinctly separated from other conduction bands, exhibit ($K\uparrow, K'\downarrow$) [($K\uparrow, K\downarrow$)] with the band Chern numbers $C = (1, -1)$ [$C = (1, 1)$], corresponding to the state #3(QSH) [#1(QAH)] in Table I. Because our HF Hamiltonian maintains symmetry for spin flipping for each valley, these two results imply that the QAH, QSH, and QVH states in Table I are all the degenerate ground states. (For example, the state #5(QVH) is obtained by flipping the spin for K' in the state #3.)

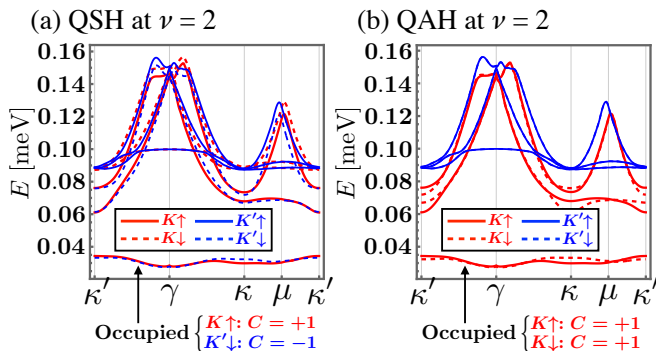


FIG. 2. Band structures at $\nu = 2$ of the lowest energy HF solutions. The Greek letters represent the high-symmetric points in the moiré Brillouin zone. Both figures provide the same many-body energy. The colors and line types indicate the valley and spin. (a) and (b) correspond to the states #3(QSH) and #1(QAH) in Table I. In the HF calculation in (b), we introduce a small “valley Zeeman term” to favor the valley K (see footnote [81]).

Lowest energy state — Now, we examine the selectivity among the QAH, QSH, and QVH states in Table I under three conditions: (I) In-plane magnetic field, (II) out-of-plane magnetic field, and (III) no magnetic field.

(I) *In-plane magnetic field*: This magnetic field favors a state with the largest in-plane magnetization, which is the QVH state due to the spin-polarization. The strength of the spin magnetization for each state is $M_{\text{spin}}^{(\text{QVH})} = g\mu_B n_e$ and $M_{\text{spin}}^{(\text{QAH})} = M_{\text{spin}}^{(\text{QSH})} = 0$, where the g -factor is set to 2, μ_B is the Bohr magneton, and n_e is the electron density. Note that in-plane component of the orbital magnetization is absent.

(II) *Out-of-plane magnetic field*: Unlike the in-plane field, the relevant magnetization is both spin and orbital ones. The orbital magnetization in z -direction is calculated by [82–85]

$$M_{\text{orb}}^z = \frac{e}{2\hbar i} \int^\mu \frac{dk^2}{(2\pi)^2} \left\langle \frac{\partial u}{\partial \mathbf{k}} \right| \times (H(\mathbf{k}) + E(\mathbf{k}) - 2\mu) \left| \frac{\partial u}{\partial \mathbf{k}} \right\rangle, \quad (1)$$

where $u(\mathbf{k})$ and $E(\mathbf{k})$ are an eigenstate and eigenenergy of a Bloch Hamiltonian $H(\mathbf{k})$, respectively. The integral is taken over states with energies below the chemical potential μ . (In the numerical calculation, μ is taken at the top of the valence bands.) In Fig. 3, we plot M_{orb}^z of the states #1 and #3 in Table I as representatives for the QAH and QSH states. The QVH state exhibits the same M_{orb}^z as that of the QSH state due to symmetry. The scaling analysis in the figure demonstrates that the QSH state exhibits no magnetization, $M_{\text{orb}}^{z(\text{QSH})} + M_{\text{spin}}^{(\text{QSH})} = 0$, and the QAH state has about five times larger magneti-

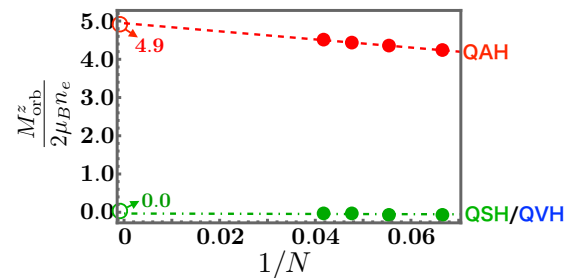


FIG. 3. Orbital magnetization M_{orb}^z quoted in units of $2\mu_B n_e$, where μ_B is the Bohr magneton and n_e is the electron density. Here $N \times N$ moiré unit cells are considered. We use the states #1 and #3 in Table I as representatives for the QAH and QSH states. The dashed lines are the linear approximation. The QSH and QVH states exhibits the same M_{orb}^z due to symmetry.

zation than that of the QVH state:

$$\frac{M_{\text{orb}}^{z(\text{QAH})} + M_{\text{spin}}^{(\text{QAH})}}{M_{\text{orb}}^{z(\text{QVH})} + M_{\text{spin}}^{(\text{QVH})}} \approx 4.9 \equiv \alpha. \quad (2)$$

Thus, the QAH state becomes favored for the out-of-plane magnetic field.

(III) *No magnetic field*: In this case, a state with the smallest magnetization emerges to minimize magnetostatic energy. Therefore, the QSH state becomes favored. (At this moment, we cannot energetically differentiate the states #3 and #4 in Table I. However, either state should be favored when considering weak spin-orbit interactions in real systems.)

The above argument implies that the QSH state, realized in the absence of a magnetic field, transitions to the QVH or QAH states by applying a magnetic field. Moreover, the QVH and QAH states can be switched by tilting the field. In Fig. 1, we summarize which state has the lowest energy as a function of both in-plane and out-of-plane components (B_{\parallel}, B_{\perp}). The only unknown parameter in the figure is the critical field B_C , defined so that $B_C \times M_{\text{orb}}^{z(\text{QAH})}$ equals the magnetostatic energy of the QAH state. Some boundaries involve valley flips, representing the first-order transitions. We discuss resulting hysteresis scans of the charge and spin Hall conductances in Sec. S4 of SM [79].

Interlocking structure in charge density — So far our focus has been on the QAH, QSH, and QVH states. Now, we explore other competitive states.

Figure 4(a) presents the HF band structure of a metastable solution at $\nu = 2$. The difference in many-body energy from the lowest energy state, that is Fig. 2(a), is about 0.00015meV per particle. Although both band structures are quite similar, one band in Fig. 4(a) carries a zero band Chern number.

The two lowest bands in Fig. 4(a) have crystal density structures exhibiting an interlocking shape. As shown

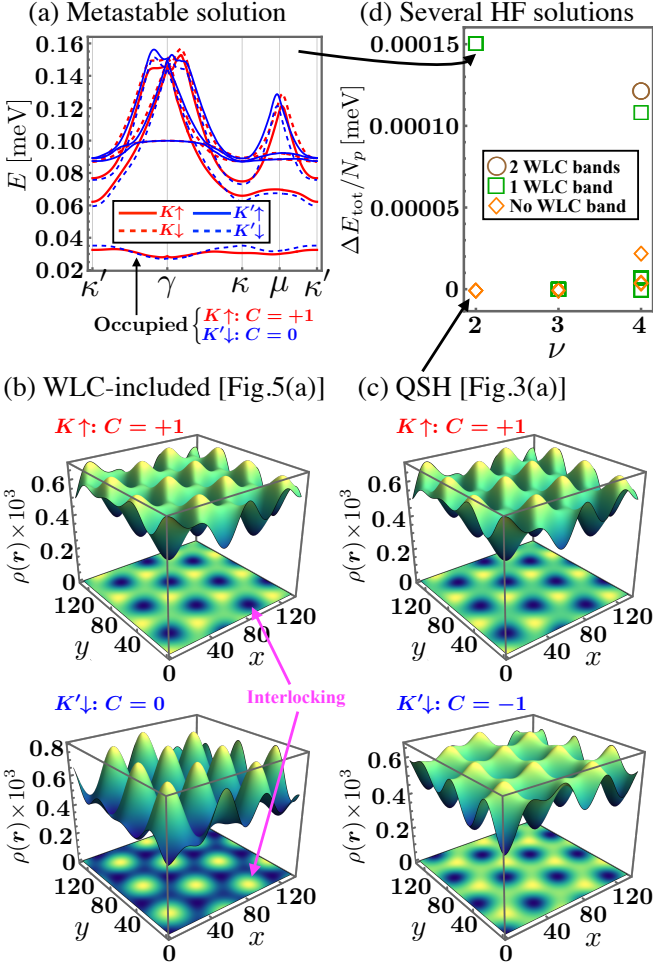


FIG. 4. (a) HF band structure of a metastable solution at $\nu = 2$. One of the two lowest bands carries $C = 0$. (b)(c) Charge density $\rho(\mathbf{r})$. The position $\mathbf{r} = (x, y)$ is measured in units of the lattice constant of graphene a_G . The figures in (b) and (c) correspond to the two lowest bands in Figs. 4(a) and 2(a), respectively. Bands with $|C| = 1$ ($C = 0$) have an extended (localized) structure in the densities. The light (dark) color indicates the high (low) density area. (d) The HF calculations are performed with 10–20 randomized initial states. We plot the difference in the many-body energy per particle relative to the lowest value at each ν . (There seem to be a few plots because of the degeneracy.) The color of plots indicates the number of trivial bands, called WLC bands.

in Fig. 4(b), the density $\rho(\mathbf{r})$ of the Chern band is spatially extended, while that of the trival band is localized and isolated from each other in a triangular lattice like Wigner-like crystal (WLC) [33, 34]. Remarkably, each localized density in the trival band is accommodated to a low density area of the Chern band. We now call this state as the “WLC-included state”. For comparison, in Fig. 4(c), we plot $\rho(\mathbf{r})$ of the QSH state in Fig. 2(a). The two Chern bands present similar (but shifted) extended structures. Note that even though the interlocking shape in Fig. 4(b) appears more stable, the WLC-included state

TABLE II. Spin and orbital magnetizations, M_{spin} and M_{orb}^z , for the low-energy states in Fig. 4(d). The magnetizations M_{spin} and M_{orb}^z are in units of $2\mu_B n_e$.

ν	Type	$\Delta E_{\text{tot}}/N_p$ [meV]	M_{spin}	$ M_{\text{orb}}^z $
	$\text{PH}_{\nu=1}$	0	1/3	1.5
3	$\text{WLC} \otimes \text{QAH}$	$\lesssim 10^{-6}$	1/3	2.8
	$\text{WLC} \otimes \text{QSH}$		1/3	0.3
	$\text{WLC} \otimes \text{QVH}$		1/3	0.3
4	$\text{WLC} \otimes \text{PH}_{\nu=1}$	0	0	0.9
	$\text{PH}_{\nu=0}$	$5. \times 10^{-6}$	0	0.0

is not the lowest energy state. This implies that forming the WLC requires more energy than the advantage gained from the interlocking shape.

Lowest energy states at $\nu = 3$ and 4 — From the analogy of $\nu = 2$, one may expect that the ground states at $\nu = 3$ and 4 occupy only the Chern bands, corresponding to the particle-hole counterpart of the $\nu = 1$ and 0 ground state within the Chern band subspace (we call these states the $\text{PH}_{\nu=1}$ and $\text{PH}_{\nu=0}$ states, respectively). However, we demonstrate that this is not always true; the WLC-included state may yield the lowest energy. In Fig. 4(d), we perform the HF calculations with 10–20 randomized initial states at $\nu = 2, 3, 4$, and plot the many-body energy difference relative to the lowest value, denoted by ΔE_{tot} . The color represents the number of occupied trivial bands, called the WLC band. The ground state at $\nu = 3$ has no WLC band, which is the $\text{PH}_{\nu=1}$ state, but the energy difference with the WLC-included state is much smaller than that at $\nu = 2$. Crucially, at $\nu = 4$, the ground state is the WLC-included state. These results imply that as ν increases, the interlocking structures becomes more advantageous, making the WLC-included state at $\nu = 4$ lower in energy than the $\text{PH}_{\nu=0}$ state. (The band structures and densities at $\nu = 3$ and 4 are presented in Sec. S5 of SM [79].)

Before closing, let us discuss the phases realized at $\nu = 3$ and 4 with or without magnetic fields. Table II shows the spin and orbital magnetizations of the low-energy states in Fig. 4(d). Both at $\nu = 3$ and 4, the ground state of the HF Hamiltonian, that is $\Delta E_{\text{tot}} = 0$, exhibit finite magnetization; conversely, the states with the smallest magnetization (i.e., the lowest magnetostatic energy) have a finite ΔE_{tot} . Therefore, either state can be the lowest energy state in the absence of a magnetic field, depending on the ratio of ΔE_{tot} to the magnetostatic energy. If one applies an out-of-plane magnetic field with a sufficiently large amplitude, the system will transition to the state with the largest $|M_{\text{orb}}^z|$, which is the $\text{WLC} \otimes \text{QAH}$ ($\text{WLC} \otimes \text{PH}_{\nu=1}$) state at $\nu = 3$ (4).

Concluding remarks — In this Letter, we have demonstrated that many-body effects triggers competi-

tion among three topologically distinct states – the QAH, QSH, and QVH states – in pentalayer rhombohedral graphene on hBN at $\nu = 2$. Without a magnetic field, the QSH phase with zero magnetization is favored due to minimal magnetostatic energy. In-/out-of-plane magnetic fields, however, favor the QAH/QVH states. Therefore, switching between the three phases can be achieved by applying and tilting a magnetic field. Furthermore, we have shown that incorporating the WLC state can produce the lowest energy state at $\nu = 3$ and 4. Therefore, the realized phases are not necessarily equivalent to the particle-hole counterparts of $4 - \nu = 1$ and 0 within the Chern band subspace. This allows for the emergence of several topological phases.

Recently, it has been proposed that composite fermions (CFs) [86, 87] form in twisted bilayer MoTe_2 even without an external magnetic field [25, 26]. Generally, the CF theory establishes a mapping between the multi-component fractional and integer quantum Hall effects [87–89]. If the CF picture holds valid in pentalayer rhombohedral graphene on hBN, our findings would also contribute to the fractional QAH physics.

The work is supported in part by JSPS KAKENHI Grant nos. JP23K19036, JP24K06926, JP20H01830, and JST CREST Grant no. JPMJCR18T2.

-
- [1] J. Cai, E. Anderson, C. Wang, X. Zhang, X. Liu, W. Holtzmann, Y. Zhang, F. Fan, T. Taniguchi, K. Watanabe, et al., *Nature* **622**, 63 (2023), URL <https://doi.org/10.1038/s41586-023-06289-w>.
- [2] Y. Zeng, Z. Xia, K. Kang, J. Zhu, P. Knüppel, C. Vaswani, K. Watanabe, T. Taniguchi, K. F. Mak, and J. Shan, *Nature* **622**, 69 (2023), URL <https://doi.org/10.1038/s41586-023-06452-3>.
- [3] H. Park, J. Cai, E. Anderson, Y. Zhang, J. Zhu, X. Liu, C. Wang, W. Holtzmann, C. Hu, Z. Liu, et al., *Nature* **622**, 74 (2023).
- [4] F. Xu, Z. Sun, T. Jia, C. Liu, C. Xu, C. Li, Y. Gu, K. Watanabe, T. Taniguchi, B. Tong, et al., *Phys. Rev. X* **13**, 031037 (2023), URL <https://link.aps.org/doi/10.1103/PhysRevX.13.031037>.
- [5] Z. Lu, T. Han, Y. Yao, A. P. Reddy, J. Yang, J. Seo, K. Watanabe, T. Taniguchi, L. Fu, and L. Ju, *Nature* **626**, 759 (2024), ISSN 1476-4687, URL <https://doi.org/10.1038/s41586-023-07010-7>.
- [6] E. Y. Andrei and A. H. MacDonald, *Nature Materials* **19**, 1265 (2020), URL <https://doi.org/10.1038/s41563-020-00840-0>.
- [7] K. F. Mak and J. Shan, *Nature Nanotechnology* **17**, 686 (2022), URL <https://doi.org/10.1038/s41565-022-01165-6>.
- [8] Y. Cao, V. Fatemi, S. Fang, K. Watanabe, T. Taniguchi, E. Kaxiras, and P. Jarillo-Herrero, *Nature* **556**, 43 (2018), URL <https://doi.org/10.1038/nature26160>.
- [9] A. L. Sharpe, E. J. Fox, A. W. Barnard, J. Finney, K. Watanabe, T. Taniguchi, M. A. Kastner, and D. Goldhaber-Gordon, *Science* **365**, 605 (2019), URL <https://www.science.org/doi/pdf/10.1126/science.aaw3780>, URL <https://www.science.org/doi/abs/10.1126/science.aaw3780>.
- [10] H. Li, S. Li, E. C. Regan, D. Wang, W. Zhao, S. Kahn, K. Yumigeta, M. Blei, T. Taniguchi, K. Watanabe, et al., *Nature* **597**, 650 (2021), URL <https://doi.org/10.1038/s41586-021-03874-9>.
- [11] C. Jin, Z. Tao, T. Li, Y. Xu, Y. Tang, J. Zhu, S. Liu, K. Watanabe, T. Taniguchi, J. C. Hone, et al., *Nature Materials* **20**, 940 (2021), URL <https://doi.org/10.1038/s41563-021-00959-8>.
- [12] E. Anderson, F.-R. Fan, J. Cai, W. Holtzmann, T. Taniguchi, K. Watanabe, D. Xiao, W. Yao, and X. Xu, *Science* **381**, 325 (2023), URL <https://www.science.org/doi/pdf/10.1126/science.adg4268>, URL <https://www.science.org/doi/abs/10.1126/science.adg4268>.
- [13] C. R. Dean, L. Wang, P. Maher, C. Forsythe, F. Ghahari, Y. Gao, J. Katoch, M. Ishigami, P. Moon, M. Koshino, et al., *Nature* **497**, 598 (2013), URL <https://doi.org/10.1038/nature12186>.
- [14] E. M. Spanton, A. A. Zibrov, H. Zhou, T. Taniguchi, K. Watanabe, M. P. Zaletel, and A. F. Young, *Science* **360**, 62 (2018), URL <https://www.science.org/doi/pdf/10.1126/science.aan8458>, URL <https://www.science.org/doi/abs/10.1126/science.aan8458>.
- [15] J. Liu, Z. Ma, J. Gao, and X. Dai, *Phys. Rev. X* **9**, 031021 (2019), URL <https://link.aps.org/doi/10.1103/PhysRevX.9.031021>.
- [16] K. Kang, B. Shen, Y. Qiu, K. Watanabe, T. Taniguchi, J. Shan, and K. F. Mak, *Observation of the fractional quantum spin hall effect in moiré mottel* (2024), 2402.03294.
- [17] K. Kang, Y. Qiu, K. Watanabe, T. Taniguchi, J. Shan, and K. F. Mak, *Observation of the double quantum spin hall phase in moiré wse2* (2024), 2402.04196.
- [18] Z. Liu and E. J. Bergholtz, in *Encyclopedia of Condensed Matter Physics (Second Edition)*, edited by T. Chakraborty (Academic Press, Oxford, 2024), pp. 515–538, second edition ed., ISBN 978-0-323-91408-6, URL <https://www.sciencedirect.com/science/article/pii/B9780323908009001360>.
- [19] M. Serlin, C. L. Tschirhart, H. Polshyn, Y. Zhang, J. Zhu, K. Watanabe, T. Taniguchi, L. Balents, and A. F. Young, *Science* **367**, 900 (2020), URL <https://www.science.org/doi/pdf/10.1126/science.aay5533>, URL <https://www.science.org/doi/abs/10.1126/science.aay5533>.
- [20] Y. Deng, Y. Yu, M. Z. Shi, Z. Guo, Z. Xu, J. Wang, X. H. Chen, and Y. Zhang, *Science* **367**, 895 (2020), URL <https://www.science.org/doi/pdf/10.1126/science.aax8156>, URL <https://www.science.org/doi/abs/10.1126/science.aax8156>.
- [21] T. Li, S. Jiang, B. Shen, Y. Zhang, L. Li, Z. Tao, T. Devakul, K. Watanabe, T. Taniguchi, L. Fu, et al., *Nature* **600**, 641 (2021), URL <https://doi.org/10.1038/s41586-021-04171-1>.
- [22] B. A. Foutty, C. R. Kometter, T. Devakul, A. P. Reddy, K. Watanabe, T. Taniguchi, L. Fu, and B. E. Feldman, *Science* **384**, 343 (2024), URL <https://www.science.org/doi/pdf/10.1126/science.adi4728>, URL <https://www.science.org/doi/abs/10.1126/science.adi4728>.

- science.adi4728.
- [23] A. P. Reddy, F. Alsallom, Y. Zhang, T. Devakul, and L. Fu, Phys. Rev. B **108**, 085117 (2023), URL <https://link.aps.org/doi/10.1103/PhysRevB.108.085117>.
- [24] C. Wang, X.-W. Zhang, X. Liu, Y. He, X. Xu, Y. Ran, T. Cao, and D. Xiao, Phys. Rev. Lett. **132**, 036501 (2024), URL <https://link.aps.org/doi/10.1103/PhysRevLett.132.036501>.
- [25] J. Dong, J. Wang, P. J. Ledwith, A. Vishwanath, and D. E. Parker, Phys. Rev. Lett. **131**, 136502 (2023), URL <https://link.aps.org/doi/10.1103/PhysRevLett.131.136502>.
- [26] H. Goldman, A. P. Reddy, N. Paul, and L. Fu, Phys. Rev. Lett. **131**, 136501 (2023), URL <https://link.aps.org/doi/10.1103/PhysRevLett.131.136501>.
- [27] A. P. Reddy and L. Fu, Toward a global phase diagram of the fractional quantum anomalous Hall effect (2023), 2308.10406.
- [28] C. Xu, J. Li, Y. Xu, Z. Bi, and Y. Zhang, Proceedings of the National Academy of Sciences **121**, e2316749121 (2024), <https://www.pnas.org/doi/pdf/10.1073/pnas.2316749121>, URL <https://www.pnas.org/doi/abs/10.1073/pnas.2316749121>.
- [29] T. Wang, T. Devakul, M. P. Zaletel, and L. Fu, Topological magnets and magnons in twisted bilayer mote_2 (2023), 2306.02501.
- [30] J. Yu, J. Herzog-Arbeitman, M. Wang, O. Vafek, B. A. Bernevig, and N. Regnault, Fractional chern insulators vs. non-magnetic states in twisted bilayer mote_2 (2023), 2309.14429.
- [31] Z. Dong, A. S. Patri, and T. Senthil, Theory of fractional quantum anomalous hall phases in pentalayer TaCl_5 (2023), 2311.03445.
- [32] B. Zhou, H. Yang, and Y.-H. Zhang, Fractional quantum anomalous hall effects in rhombohedral TaCl_5 (2023), 2311.04217.
- [33] J. Dong, T. Wang, T. Wang, T. Soejima, M. P. Zaletel, A. Vishwanath, and D. E. Parker, Anomalous hall crystals in rhombohedral multilayer graphene i: TaCl_5 (2023), 2311.05568.
- [34] Y. H. Kwan, J. Yu, J. Herzog-Arbeitman, D. K. Efetov, N. Regnault, and B. A. Bernevig, Moiré fractional chern insulators iii: Hartree-fock phase diagram, TaCl_5 (2023), 2312.11617.
- [35] J. Herzog-Arbeitman, Y. Wang, J. Liu, P. M. Tam, Z. Qi, Y. Jia, D. K. Efetov, O. Vafek, N. Regnault, H. Weng, et al., Moiré fractional chern insulators ii: First-principles calculation (2023), 2311.12920.
- [36] Z. Guo, X. Lu, B. Xie, and J. Liu, Theory of fractional chern insulator states in pentalayer graphene (2023), 2311.14368.
- [37] Z. Liu and J. Wang, Layer-dependent quantum anomalous hall effect in rhombohedral TaCl_5 (2024), 2401.13413.
- [38] Y. Zeng, D. Guerci, V. Crépel, A. J. Millis, and J. Cano, Sublattice structure and topology in spontaneously crystallized electron gases (2024), 2402.17867.
- [39] T. Tan and T. Devakul, Parent berry curvature and the ideal anomalous hall crystal (2024), 2403.04196.
- [40] T. Soejima, J. Dong, T. Wang, T. Wang, M. P. Zaletel, A. Vishwanath, and D. E. Parker, Anomalous hall crystals in rhombohedral multilayer graphene ii: TaCl_5 (2024), 2403.05522.
- [41] Z. Dong, A. S. Patri, and T. Senthil, Stability of anomalous hall crystals in multilayer rhombohedral graphene (2024), 2403.07873.
- [42] M. Xie and S. D. Sarma, Integer and fractional quantum anomalous hall effects in pentalayer TaCl_5 (2024), 2404.02192.
- [43] D. N. Sheng, A. P. Reddy, A. Abouelkomsan, E. J. Bergholtz, and L. Fu, Quantum anomalous hall crystal at fractional filling of moiré superlattice (2024), 2402.17832.
- [44] H. Lu, H.-Q. Wu, B.-B. Chen, and Z. Y. Meng, Direct transition from a fractional quantum anomalous hall state to a normal state (2024), 2404.06745.
- [45] K. P. Nuckolls and A. Yazdani, Unified perspective on moiré materials (2024), 2404.08044.
- [46] H. Zhou, T. Xie, A. Ghazaryan, T. Holder, J. R. Ehrets, E. M. Spanton, T. Taniguchi, K. Watanabe, E. Berg, M. Serbyn, et al., Nature **598**, 429 (2021), URL <https://doi.org/10.1038/s41586-021-03938-w>.
- [47] H. Zhou, T. Xie, T. Taniguchi, K. Watanabe, and A. F. Young, Nature **598**, 434 (2021), URL <https://doi.org/10.1038/s41586-021-03926-0>.
- [48] H. Zhou, L. Holleis, Y. Saito, L. Cohen, W. Huynh, C. L. Patterson, F. Yang, T. Taniguchi, K. Watanabe, and A. F. Young, Science **375**, 774 (2022), <https://www.science.org/doi/pdf/10.1126/science.abm8386>, URL <https://www.science.org/doi/abs/10.1126/science.abm8386>.
- [49] S. C. de la Barrera, S. Aronson, Z. Zheng, K. Watanabe, T. Taniguchi, Q. Zhang, and R. Ashoori, Nature Physics **18**, 771 (2022), URL <https://doi.org/10.1038/s41567-022-01616-w>.
- [50] Y. Zhang, R. P. Dijk, A. S. F. Thomson, and J. C. Duda, Printed superlattice in TaCl_5 (2023), 2311.05446.
- [51] T. Han, Z. Lu, G. Scuri, J. Sung, J. Wang, T. Han, K. Watanabe, T. Taniguchi, L. Fu, H. Park, et al., Nature **623**, 41 (2023), URL <https://doi.org/10.1038/s41586-023-06572-w>.
- [52] T. Han, Z. Lu, G. Scuri, J. Sung, J. Wang, T. Han, K. Watanabe, T. Taniguchi, H. Park, and L. Ju, Nature Nanotechnology **19**, 181 (2024), URL <https://doi.org/10.1038/s41565-023-01520-1>.
- [53] Y. Ren, K. Watanabe, T. Taniguchi, J. Jia, et al., Interaction-driven spontaneous broken-symmetry insulator and metal in TaCl_5 (2023), 2306.14042.
- [54] M. Das and C. Huang, Superpolarized electron-hole liquid and multiferroicity in multilayer TaCl_5 (2024), 2404.10069.
- [55] T. Han, Z. Lu, Y. Yao, J. Yang, J. Seo, C. Yoon, K. Watanabe, T. Taniguchi, L. Fu, E. Zhang, et al., Science **384**, 647 (2024), <https://www.science.org/doi/pdf/10.1126/science.adk9749>, URL <https://www.science.org/doi/abs/10.1126/science.adk9749>.
- [56] J. Xie, Z. Huo, X. Lu, Z. Feng, Z. Zhang, W. Wang, Q. Yang, K. Watanabe, T. Taniguchi, K. Liu, et al., Even- and odd-denominator fractional quantum anomalous hall effect

- (2024), 2405.16944.
- [57] F. Guinea, A. H. Castro Neto, and N. M. R. Peres, Phys. Rev. B **73**, 245426 (2006), URL <https://link.aps.org/doi/10.1103/PhysRevB.73.245426>.
- [58] P. Moon and M. Koshino, Phys. Rev. B **90**, 155406 (2014), URL <https://link.aps.org/doi/10.1103/PhysRevB.90.155406>.
- [59] J. Jung, A. Raoux, Z. Qiao, and A. H. MacDonald, Phys. Rev. B **89**, 205414 (2014), URL <https://link.aps.org/doi/10.1103/PhysRevB.89.205414>.
- [60] K. v. Klitzing, G. Dorda, and M. Pepper, Phys. Rev. Lett. **45**, 494 (1980), URL <http://link.aps.org/doi/10.1103/PhysRevLett.45.494>.
- [61] R. B. Laughlin, Phys. Rev. B **23**, 5632 (1981), URL <http://link.aps.org/doi/10.1103/PhysRevB.23.5632>.
- [62] D. J. Thouless, M. Kohmoto, M. P. Nightingale, and M. den Nijs, Phys. Rev. Lett. **49**, 405 (1982), URL <http://link.aps.org/doi/10.1103/PhysRevLett.49.405>.
- [63] D. C. Tsui, H. L. Stormer, and A. C. Gossard, Phys. Rev. Lett. **48**, 1559 (1982), URL <http://link.aps.org/doi/10.1103/PhysRevLett.48.1559>.
- [64] R. B. Laughlin, Phys. Rev. Lett. **50**, 1395 (1983), URL <http://link.aps.org/doi/10.1103/PhysRevLett.50.1395>.
- [65] A. K. Geim and K. S. Novoselov, Nature Materials **6**, 183 (2007), URL <https://doi.org/10.1038/nmat1849>.
- [66] K. S. Novoselov, A. K. Geim, S. V. Morozov, D. Jiang, M. I. Katsnelson, I. V. Grigorieva, S. V. Dubonos, and A. A. Firsov, Nature **438**, 197 (2005), URL <https://doi.org/10.1038/nature04233>.
- [67] Y. Zhang, Y.-W. Tan, H. L. Stormer, and P. Kim, Nature **438**, 201 (2005), URL <https://doi.org/10.1038/nature04235>.
- [68] K. Nomura and A. H. MacDonald, Phys. Rev. Lett. **96**, 256602 (2006), URL <http://link.aps.org/doi/10.1103/PhysRevLett.96.256602>.
- [69] V. M. Apalkov and T. Chakraborty, Phys. Rev. Lett. **97**, 126801 (2006), URL <http://link.aps.org/doi/10.1103/PhysRevLett.97.126801>.
- [70] C. Töke, P. E. Lammert, V. H. Crespi, and J. K. Jain, Phys. Rev. B **74**, 235417 (2006), URL <http://link.aps.org/doi/10.1103/PhysRevB.74.235417>.
- [71] X. Du, I. Skachko, F. Duerr, A. Luican, and E. Y. Andrei, Nature **462**, 192 EP (2009), URL <http://dx.doi.org/10.1038/nature08522>.
- [72] K. I. Bolotin, F. Ghahari, M. D. Shulman, H. L. Stormer, and P. Kim, Nature **462**, 196 (2009), URL <https://doi.org/10.1038/nature08582>.
- [73] F. D. M. Haldane, Phys. Rev. Lett. **61**, 2015 (1988), URL <https://link.aps.org/doi/10.1103/PhysRevLett.61.2015>.
- [74] T. Neupert, L. Santos, C. Chamon, and C. Mudry, Phys. Rev. Lett. **106**, 236804 (2011), URL <https://link.aps.org/doi/10.1103/PhysRevLett.106.236804>.
- [75] D. N. Sheng, Z.-C. Gu, K. Sun, and L. Sheng, Nature Comm. **2**, 389 (2011), URL <http://dx.doi.org/10.1038/ncomms1380>.
- [76] N. Regnault and B. A. Bernevig, Phys. Rev. X **1**, 021014 (2011), URL <https://link.aps.org/doi/10.1103/PhysRevX.1.021014>.
- [77] K. Sun, Z. Gu, H. Katsura, and S. Das Sarma, Phys. Rev. Lett. **106**, 236803 (2011), URL <https://link.aps.org/doi/10.1103/PhysRevLett.106.236803>.
- [78] S. Raghu, X.-L. Qi, C. Honerkamp, and S.-C. Zhang, Phys. Rev. Lett. **100**, 156401 (2008), URL <https://link.aps.org/doi/10.1103/PhysRevLett.100.156401>.
- [79] See Supplemental Material for details of pentalayer rhombohedral graphene, moiré potentials, Hartree-Fock calculation, hysteresis, and additional numerical results at $\nu = 3$ and 4. This includes Refs. 90 and 91.
- [80] Y. Park, Y. Kim, B. L. Chittari, and J. Jung, Phys. Rev. B **108**, 155406 (2023), URL <https://link.aps.org/doi/10.1103/PhysRevB.108.155406>.
- [81] Our HF Hamiltonian commutes with the “valley Zeeman term”, $H_V(\mathbf{k}) = -b_V(\tau_z \otimes \sigma_0)$, where $\tau_z = \pm$ labels the valleys K and K' , and σ_0 is the identity matrix acting in the spin space. This addition merely shifts the energy at each sector. Setting b_V to be sufficiently small, we obtain Fig. 2(b). The additional energy shift [= $\pm b_z \times$ (particle number)] is excluded in the figure. In Fig. 3, we also use similar terms in order to obtain the target states, namely #1, #3, and #5.
- [82] O. Gat and J. E. Avron, Phys. Rev. Lett. **91**, 186801 (2003), URL <https://link.aps.org/doi/10.1103/PhysRevLett.91.186801>.
- [83] D. Xiao, J. Shi, and Q. Niu, Phys. Rev. Lett. **95**, 137204 (2005), URL <https://link.aps.org/doi/10.1103/PhysRevLett.95.137204>.
- [84] T. Thonhauser, D. Ceresoli, D. Vanderbilt, and R. Resta, Phys. Rev. Lett. **95**, 137205 (2005), URL <https://link.aps.org/doi/10.1103/PhysRevLett.95.137205>.
- [85] R. Nakai and K. Nomura, Phys. Rev. B **93**, 214434 (2016), URL <https://link.aps.org/doi/10.1103/PhysRevB.93.214434>.
- [86] J. K. Jain, Phys. Rev. Lett. **63**, 199 (1989), URL <http://link.aps.org/doi/10.1103/PhysRevLett.63.199>.
- [87] J. K. Jain, Composite Fermions (Cambridge University Press, New York, US, 2007).
- [88] X. G. Wu, G. Dev, and J. K. Jain, Phys. Rev. Lett. **71**, 153 (1993), URL <https://link.aps.org/doi/10.1103/PhysRevLett.71.153>.
- [89] V. W. Scarola and J. K. Jain, Phys. Rev. B **64**, 085313 (2001), URL <http://link.aps.org/doi/10.1103/PhysRevB.64.085313>.
- [90] F. Zhang, B. Sahu, H. Min, and A. H. MacDonald, Phys. Rev. B **82**, 035409 (2010), URL <https://link.aps.org/doi/10.1103/PhysRevB.82.035409>.
- [91] L. Liu, Y. P. Feng, and Z. X. Shen, Phys. Rev. B **68**, 104102 (2003), URL <https://link.aps.org/doi/10.1103/PhysRevB.68.104102>.

Supplemental Material

S1. PENTALAYER RHOMBOHEDRAL GRAPHENE

The tight-binding Hamiltonian of pentalayer rhombohedral graphene is given by [31, 33, 80, 90]

$$\tilde{h}_{\text{R5G}}(\mathbf{k}) = \begin{pmatrix} D_1 & V & W & 0 & 0 \\ V^\dagger & D_2 & V & W & 0 \\ W^\dagger & V^\dagger & D_3 & V & W \\ 0 & W^\dagger & V^\dagger & D_4 & V \\ 0 & 0 & W^\dagger & V^\dagger & D_5 \end{pmatrix} \quad (\text{S1})$$

where

$$D_l = \begin{pmatrix} 0 & t_0 g(\mathbf{k}) \\ t_0 g^*(\mathbf{k}) & 0 \end{pmatrix} + u_D (l-3) \quad (\text{S2})$$

$$V = \begin{pmatrix} t_4 g^*(\mathbf{k}) & t_1 \\ t_3 g(\mathbf{k}) & t_4 g^*(\mathbf{k}) \end{pmatrix} \quad (\text{S3})$$

$$W = \begin{pmatrix} 0 & 0 \\ t_2 & 0 \end{pmatrix} \quad (\text{S4})$$

$$g(\mathbf{k}) = \sum_{i=1}^3 e^{-i\mathbf{k}\cdot\boldsymbol{\tau}_i}. \quad (\text{S5})$$

Here, t_0 and (t_1, t_2, t_3, t_4) are the intralayer and interlayer hopping terms [see Fig. S1(a)], u_D is the interlayer potential difference induced by a perpendicular displacement field, and $\boldsymbol{\tau}_i$'s are the vectors connecting the nearest neighbor sublattices. The effective continuum Hamiltonian $h_{\text{R5G}}(\mathbf{k})$ in the main text is given by replacing $g(\mathbf{k})$ with $a_G \sqrt{3}/2(\xi k_x - i k_y)$, where a_G is the lattice constant of graphene and $\xi = +1$ (-1) for the valley K (K'). Each parameter in Fig. S1(a) is assigned as $(t_0, t_1, t_2, t_3, t_4, u_D) = (-3100, 380, -10.5, 290, 141, 50)$ meV, expected to match experimental conditions for the $\nu = 1$ QAH effect [5, 31, 33, 80].

S2. MOIRÉ POTENTIAL

We describe an effective continuum model for a moiré potential, following an approach in Ref. 58. Now, we consider the layer $l = 1$ of pentalayer rhombohedral graphene and hBN. The lattice constants of graphene and hBN are fixed as $a_G = 0.246$ nm and $a_{\text{hBN}} = 0.2504$ nm [91], inducing the lattice mismatch as $\epsilon = a_{\text{hBN}}/a_G - 1 \approx 1.8\%$. The twist angle is set to $\theta = 0.77^\circ$ to align with the experiment in Ref. 5.

Let us first derive the primitive vectors of the moiré superlattice and the corresponding reciprocal lattice vectors. We denote the primitive lattice vectors of graphene by \mathbf{a}_i with $i = 1, 2$. For hBN, we have

$$\tilde{\mathbf{a}}_i = M R \mathbf{a}_i, \quad (\text{S6})$$

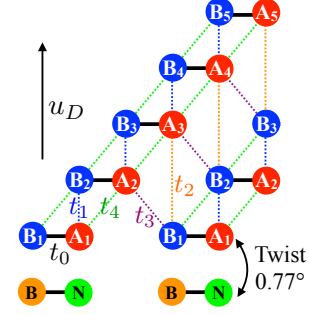


FIG. S1. (a) Pentalayer rhombohedral graphene on hBN layer. A_l and B_l are the sublattices of the l th layer. The solid and dotted lines represent intralayer t_0 and interlayer (t_1, t_2, t_3, t_4) hopping terms. The twist angle between graphene and hBN is 0.77° . A perpendicular displacement field induces the interlayer potential difference u_D .

where $M = (1 + \epsilon)\mathbf{1}$, and R is a rotation matrix by θ . This relation implies that a lattice of hBN at \mathbf{r} has its counterpart of graphene at $R^{-1}M^{-1}\mathbf{r}$. Their displacement is

$$\boldsymbol{\delta}(\mathbf{r}) = (1 - R^{-1}M^{-1})\mathbf{r}. \quad (\text{S7})$$

The primitive vectors of the moiré superlattice \mathbf{L}_i^M is defined so that $\boldsymbol{\delta}(\mathbf{L}_i^M) = \mathbf{a}_i$:

$$\mathbf{L}_i^M = (1 - R^{-1}M^{-1})^{-1}\mathbf{a}_i. \quad (\text{S8})$$

In our settings, we have $|\mathbf{L}_i^M| \approx 45.4a_G \approx 11.2$ nm. The moiré reciprocal lattice vectors, satisfying $\mathbf{L}_i^M \cdot \mathbf{G}_i^M = 2\pi\delta_{ij}$, are given by

$$\begin{aligned} \mathbf{G}_i^M &= (1 - M^{-1}R)\mathbf{a}_i^* \\ &= \mathbf{a}_i^* - \tilde{\mathbf{a}}_i^*, \end{aligned} \quad (\text{S9})$$

where \mathbf{a}_i^* and $\tilde{\mathbf{a}}_i^*$ are the reciprocal lattice vectors of graphene and hBN, satisfying $\mathbf{a}_i \cdot \mathbf{a}_j^* = \tilde{\mathbf{a}}_i \cdot \tilde{\mathbf{a}}_j^* = 2\pi\delta_{ij}$. Here, the relation $\tilde{\mathbf{a}}_i^* = M^{-1}R\mathbf{a}_i^*$ is obtained by $\mathbf{a}_i \cdot \mathbf{a}_j^* = \mathbf{a}_i^T \mathbf{a}_j^* = (R^{-1}M^{-1}\tilde{\mathbf{a}}_i)^T \mathbf{a}_j^* = \tilde{\mathbf{a}}_i^T M^{-1}R\mathbf{a}_j^*$.

The bilayer system composed of graphene and hBN is effectively described by a tight-binding lattice Hamiltonian. Eliminating the hBN bases based on the second order perturbation within an effective continuum framework, the effect of the hBN (for a given valley and spin) is represented by a local potential $v(\mathbf{r})$ within the graphene

subspace [58]:

$$v(\mathbf{r}) = V_0 \begin{pmatrix} 1 & 0 \\ 0 & 1 \end{pmatrix} + \left\{ V_1 e^{i\xi\psi} \left[\begin{pmatrix} 1 & \omega^{-\xi} \\ 1 & \omega^{-\xi} \end{pmatrix} e^{i\xi\mathbf{G}_1^M \cdot \mathbf{r}} + \begin{pmatrix} 1 & \omega^\xi \\ \omega^\xi & \omega^{-\xi} \end{pmatrix} e^{i\xi\mathbf{G}_2^M \cdot \mathbf{r}} + \begin{pmatrix} 1 & 1 \\ \omega^{-\xi} & \omega^{-\xi} \end{pmatrix} e^{-i\xi(\mathbf{G}_1^M + \mathbf{G}_2^M) \cdot \mathbf{r}} \right] + \text{H.c.} \right\}, \quad (\text{S10})$$

where $\omega = \exp\{2\pi i/3\}$ and $\xi = +1$ (-1) for the valley K (K'). Here, we use $V_0 = 28.9\text{meV}$, $V_1 = 21.0\text{meV}$ and $\psi = -0.29\text{rad}$ following Ref. 58. As mentioned in the main text, its second quantized form is

$$V_{\text{hBN}} = \sum_{\mathbf{k}} \sum_{m_1 m_2} \tilde{c}^\dagger(\mathbf{k} + m_1 \mathbf{G}_1 + m_2 \mathbf{G}_2) v(m_1, m_2) \tilde{c}(\mathbf{k}) \quad (\text{S11})$$

where $\tilde{c}^\dagger = (c_{A_1}^\dagger, c_{B_1}^\dagger)$ and $v(m_1, m_2)$ is the Fourier coefficient of $v(\mathbf{r})$. In the numerical calculations, the summation $\sum_{\mathbf{k}} \sum_{m_1 m_2}$ is confined to the first and second moiré Brillouin zones.

S3. HARTREE-FOCK CALCULATION

Let us describe the self-consistent HF calculation. As mentioned in the main text, the interaction before the mean-field approximation has the form of

$$H_{\text{int}} = \frac{1}{2S} \sum_{\mathbf{k}\mathbf{k}'\mathbf{q}} \sum_{ZZ'} V_C(\mathbf{q}) c_Z^\dagger(\mathbf{k} + \mathbf{q}) c_{Z'}^\dagger(\mathbf{k}' - \mathbf{q}) c_{Z'}(\mathbf{k}') c_Z(\mathbf{k}), \quad (\text{S12})$$

where S is the area of the system, and Z and Z' represent the spin, valley, sublattice and layer indices. Here, we set the positions of both K and K' to be the center in the folded moiré Brillouin zone for simplicity. The form of $V_C(\mathbf{q})$ is written in the main text. We then construct the Hartree and Fock Hamiltonians as

$$H_{\text{H}} = \frac{1}{S} \sum_{\mathbf{k}\mathbf{k}'\mathbf{q}} \sum_{ZZ'} V_C(\mathbf{q}) \left\langle c_{Z'}^\dagger(\mathbf{k}' - \mathbf{q}) c_{Z'}(\mathbf{k}') \right\rangle \times c_Z^\dagger(\mathbf{k} + \mathbf{q}) c_Z(\mathbf{k}), \quad (\text{S13})$$

$$H_{\text{F}} = -\frac{1}{S} \sum_{\mathbf{k}\mathbf{k}'\mathbf{q}} \sum_{ZZ'} V_C(\mathbf{q}) \left\langle c_{Z'}^\dagger(\mathbf{k}' - \mathbf{q}) c_Z(\mathbf{k}) \right\rangle \times c_Z^\dagger(\mathbf{k} + \mathbf{q}) c_{Z'}(\mathbf{k}'), \quad (\text{S14})$$

where $\langle \cdot \rangle$ represents the expectation value for the ground state. Now, we pick up terms that couple momenta modulo the moiré reciprocal lattice vectors. In other words, using a set of reciprocal lattice vectors of the moiré superlattice, denoted \mathbf{G} , we add constraints $\mathbf{k} + \mathbf{q} = \mathbf{k} + \mathbf{G}$

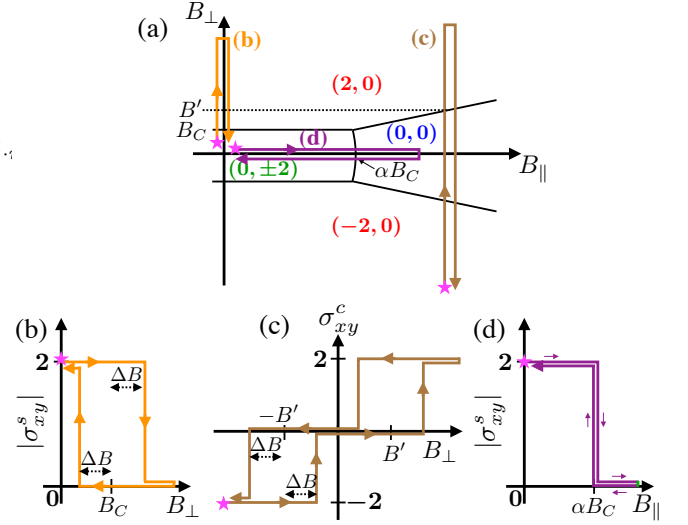


FIG. S2. (a) The same as Fig. 1. The three paths under consideration are illustrated, labeled by subsequent panels. The charge and spin Chern numbers (C_c, C_s) for each region are highlighted in red for QAH, green for QSH, and blue for QVH states. The magenta stars indicate the initial points of each path. (b)(c)(d) Charge and spin Hall conductances σ_{xy}^c and $|\sigma_{xy}^s|$. The coercive field in (b)(c) is represented by ΔB .

and $\mathbf{k} + \mathbf{q} = \mathbf{k}' + \mathbf{G}$ in Eqs. (S13) and (S14), respectively:

$$H_{\text{H}} \rightarrow \frac{1}{S} \sum_{\mathbf{k}\mathbf{k}'\mathbf{G}} \sum_{ZZ'} V_C(\mathbf{G}) \left\langle c_{Z'}^\dagger(\mathbf{k}' - \mathbf{G}) c_{Z'}(\mathbf{k}') \right\rangle \times c_Z^\dagger(\mathbf{k} + \mathbf{G}) c_Z(\mathbf{k}), \quad (\text{S15})$$

$$H_{\text{F}} \rightarrow -\frac{1}{S} \sum_{\mathbf{k}\mathbf{k}'\mathbf{G}} \sum_{ZZ'} V_C(\mathbf{k}' - \mathbf{k} + \mathbf{G}) \left\langle c_{Z'}^\dagger(\mathbf{k} - \mathbf{G}) c_Z(\mathbf{k}) \right\rangle \times c_Z^\dagger(\mathbf{k}' + \mathbf{G}) c_{Z'}(\mathbf{k}'), \quad (\text{S16})$$

In the numerical calculation, the summation $\sum_{\mathbf{k}\mathbf{k}'\mathbf{G}}$ is confined to the first and second moiré Brillouin zones. When seeking the ground state of the HF Hamiltonian for a given system parameters, we perform the self-consistent calculations with 10–20 randomized initial states.

S4. HYSTERESIS

We discuss hysteresis scans of the charge and spin Hall conductances σ_{xy}^c and σ_{xy}^s . We consider three paths in the (B_\perp, B_\parallel) space as illustrated in Fig. S2(a). (In the QSH region of the figure, the spin Chern number C_s is denoted as ± 2 to reflect the degeneracy of the states #3 and #4 in Table I. Although either state should be favored due to weak spin-orbit interactions in real systems, we simplify our argument by considering only $|\sigma_{xy}^s|$ below.)

Figures S2(b)-(d) depicts anticipated behaviors of the Hall conductance. Figures S2(b) and (c) exhibit hysteresis since transitions from the QAH to QSH/QVH states

involve valley flips, leading to a first-order transition. The coercive field ΔB in both figures is expected to be comparable to the experimentally observed one for the $\nu = 1$ QAH effect [5] because the valley of only one band needs to be flipped. Conversely, Fig. S2(d) shows no hysteresis behavior since transition from the QSH to QVH states involves only spin flips. The SU(2) spin-rotational symmetry prevents hysteresis behavior in such cases.

S5. NUMERICAL RESULTS AT $\nu = 3$ AND 4

Let us discuss the HF band structures and charge densities at $\nu = 3$ and 4. Figure S3(a) presents the band

structure of the lowest energy state at $\nu = 3$. The occupied three lowest bands are separated from other conduction bands. Each band carries the Chern number $C = +1$ or -1 depending on the valley. Their charge densities $\rho(\mathbf{r})$ are shown in Fig. S3(b). They provide similar (but shifted) extended structure.

Figure S3(c) presents the band structure of the lowest energy state at $\nu = 4$. The occupied four lowest bands are separated from other conduction bands. Three bands carry $C = +1$ or -1 while the other does $C = 0$. Their charge densities are shown Fig. S3(d). The $C = 0$ band provides the WLC density structure.

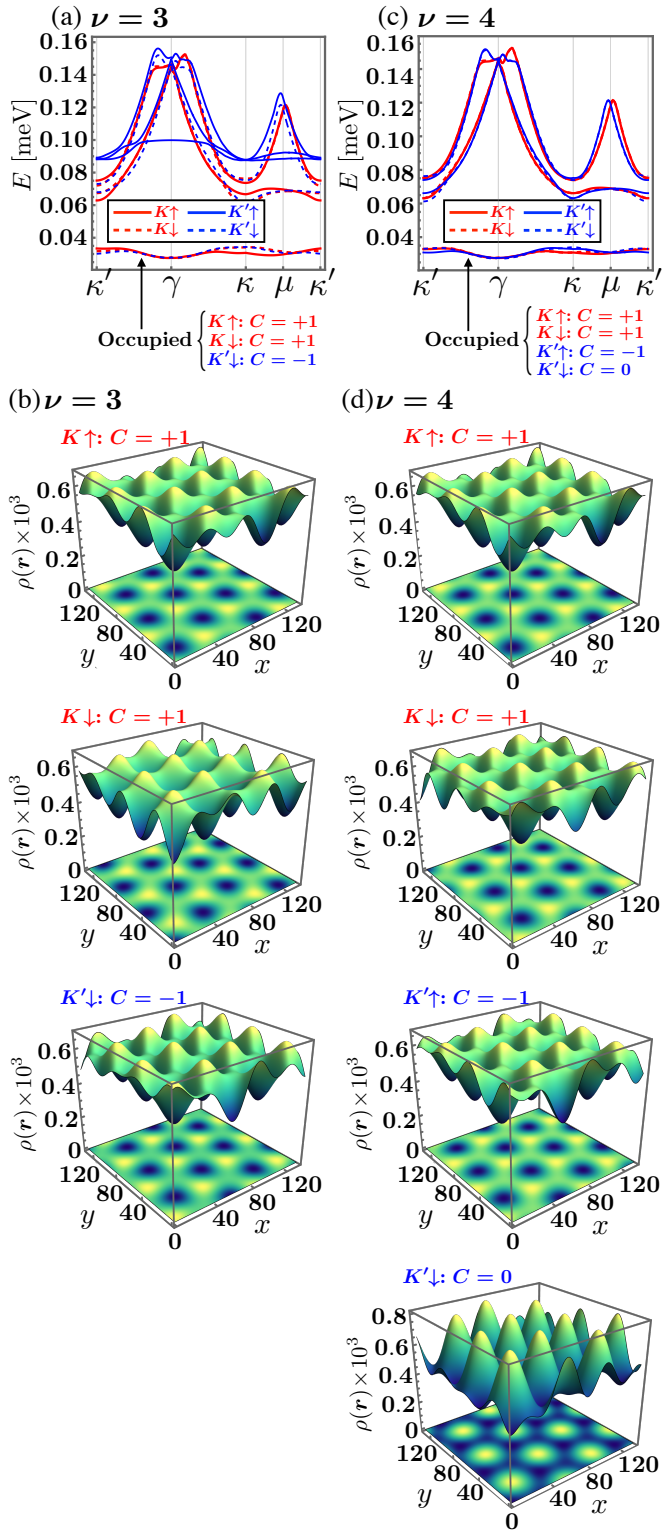


FIG. S3. (a) HF band structure at $\nu = 3$. The three lowest bands carry $C = +1$ or -1 . (b) Charge densities $\rho(\mathbf{r})$ of the three lowest bands in (a). (c) HF band structure at $\nu = 4$. One of the four lowest bands carries $C = 0$. (d) Charge densities $\rho(\mathbf{r})$ of the four lowest bands in (c).